CHALMERS
UNIVERSITY OF TECHNOLOGY

Micro- and nanostructure specific X-ray tomography reveals less matrix formation and altered collagen organization following reduced loading

Acta Biomaterialia 174 (2024) 245–257

Contents lists available at ScienceDirect

Acta Biomaterialia

journal homepage: www.elsevier.com/locate/actbio

Full length article

Micro- and nanostructure specific X-ray tomography reveals less matrix formation and altered collagen organization following reduced loading during Achilles tendon healing

Isabella Silva Barreto[a,1,*], Maria Pierantoni[a,1], Leonard C. Nielsen[b], Malin Hammerman[a,c], Ana Diaz[d], Vladimir Novak[d], Pernilla Eliasson[c,e], Marianne Liebi[b,d,f], Hanna Isaksson[a]

[a] Department of Biomedical Engineering, Lund University, Lund, Sweden
[b] Department of Physics, Chalmers University of Technology, Gothenburg, Sweden
[c] Department of Biomedical and Clinical Sciences, Linköping University, Linköping, Sweden
[d] Photon Science Division, Paul Scherrer Institute, Villigen PSI, Switzerland
[e] Department of Orthopaedics, Sahlgrenska University Hospital, Gothenburg, Sweden
[f] Institute of materials, Ecole Polytechnique fédérale de Lausanne (EPFL), Lausanne, Switzerland

ARTICLE INFO

Article history:
Received 7 August 2023
Revised 6 December 2023
Accepted 7 December 2023
Available online 12 December 2023

Keywords:
Hierarchical tissue structure
Fibers
Fibrils
3D organization
Phase-contrast microtomography
Small-angle X-ray scattering tensor tomography

ABSTRACT

Recovery of the collagen structure following Achilles tendon rupture is poor, resulting in a high risk for re-ruptures. The loading environment during healing affects the mechanical properties of the tendon, but the relation between loading regime and healing outcome remains unclear. This is partially due to our limited understanding regarding the effects of loading on the micro- and nanostructure of the healing tissue. We addressed this through a combination of synchrotron phase-contrast X-ray microtomography and small-angle X-ray scattering tensor tomography (SASTT) to visualize the 3D organization of microscale fibers and nanoscale fibrils, respectively. The effect of *in vivo* loading on these structures was characterized in early healing of rat Achilles tendons by comparing full activity with immobilization. Unloading resulted in structural changes that can explain the reported impaired mechanical performance. In particular, unloading led to slower tissue regeneration and maturation, with less and more disorganized collagen, as well as an increased presence of adipose tissue. This study provides the first application of SASTT on soft musculoskeletal tissues and clearly demonstrates its potential to investigate a variety of other collagenous tissues.

Statement of significance

Currently our understanding of the mechanobiological effects on the recovery of the structural hierarchical organization of injured Achilles tendons is limited. We provide insight into how loading affects the healing process by using a cutting-edge approach to for the first time characterize the 3D micro- and nanostructure of the regenerating collagen. We uncovered that, during early healing, unloading results in a delayed and more disorganized regeneration of both fibers (microscale) and fibrils (nanoscale), as well as increased presence of adipose tissue. The results set the ground for the development of further specialized protocols for tendon recovery.

1. Introduction

The incidence of acute Achilles tendon ruptures is increasing in both athletes and general population [1–3]. There is currently no consensus on optimal mechanical protocol to follow in order to facilitate tissue healing after Achilles tendon rupture [4–6] and the tendon rarely regains its pre-rupture structure and mechanical properties [4,7]. As a result, the risk of re-rupture is high [8]. Despite being widely accepted that the mechanical environment affects the tendon healing process, details on how the nano- and microstructure of the healing tissue are affected by loading are missing.

* Corresponding author at: Department of Biomedical Engineering, Lund University/LTH, Box 118, 221 00 Lund, Sweden.
E-mail address: isabella.silva_barreto@bme.lth.se (I. Silva Barreto).
[1] Joint first authors

https://doi.org/10.1016/j.actbio.2023.12.015

The smallest load bearing unit in tendons is the triple helix collagen type I molecule, which assembles into fibrils in a quarter staggered arrangement. Within fibrils, the collagen molecules are arranged at a periodic distance, called d-spacing, of approximately 67 nm. At the nanoscale fibrils assemble into micrometer-sized fibers. Tendons experience mechanical loading as they transfer muscle forces to bone, and this strongly influences their structure and composition, as well as their mechanical properties [9–12]. The mechanical adaptation in tendons stems from mechanosensitive cells (tenocytes) embedded in the collagen matrix, altering their activities such as production, remodeling and signaling in response to their loading environment [5,13,14].

After tendon rupture, the healing process is characterized by an inflammatory phase, followed by a reparative phase, which initially produces a disorganized matrix mostly made of collagen type III. As healing progresses, collagen production gradually shifts from type III to type I [4]. Immobilization during healing has been shown to impair matrix production and mechanical properties [4,15,16], whereas excessive loading can result in additional microdamage [17,18] and scar-tissue formation [16]. While the effects of reduced loading during tendon healing have been extensively studied regarding mechanical properties and cell behaviors, little is known regarding the effects on spatial and temporal regeneration of the collagen structure at the micro- and nanoscale. As mechanical properties of tendons are highly dependent on their structure, further investigation into this mechano-structural relationship is crucial.

Due to the highly periodic arrangement of collagen molecules, small-angle X-ray scattering (SAXS) has become a commonly applied technique to study nano-structural characteristics of collagen fibrils [19–24]. While this technique has been widely applied to intact tendons and other collagenous tissues, its application on healing tendons has been limited. Using 2D SAXS mapping, Khayyeri et al. [21] found that reduced loading during early healing impaired collagen structural and mechanical properties as well as tissue maturation. This study emphasized the heterogeneity of the healing process and highlighted the need for further spatial characterization in 3D. SAXS tensor tomography (SASTT) was recently developed for 3D nanostructural characterization of mineralized tissues [25,26]. As it also incorporates signal variability in the third dimension, it enables more accurate evaluation of anisotropic nanostructures. SASTT was developed and exemplified on bone tissue [27], and has to our knowledge so far only been used to study mineralized tissues [28–32], soft polymers [33] and myelinated axons in neural tissue [34]. Thus, it has not previously been applied to non-mineralized collagenous tissues such as tendons. Phase-contrast enhanced synchrotron microtomography (SR-PhC-µCT) is another emerging technique, which is highly suitable for 3D structural characterization of unmineralized tissues at the microscale and has recently been applied to study collagen fibers in different soft musculoskeletal tissues such as intact tendons [12,35-37], meniscus [38], intravertebral discs [39] and articular cartilage [40].

The aim of this study was to characterize the effect of different *in vivo* loading regimes on the 3D structural organization of regenerating rat Achilles tendons. Specifically, we aimed to evaluate this effect during the early healing process; 1, 2 and 3 weeks after injury. This was achieved through a multimodal approach of using SR-PhC-µCT to visualize the collagen fiber organization at the microscale and SASTT as well as 2D SAXS to visualize and quantify the collagen fibril organization at the nanoscale (Fig. 1). We hypothesized that reduced mechanical loading affects organization of regenerated collagen units, altering collagen alignment, amount and spatial distribution compared to loaded healing tendons.

2. Methods

2.1. Animal experiment

28 female specific pathogen free Sprague-Dawley rats (10 weeks old, weight 300 ± 20 g, from Janvier, Le Genest-Saint-Isle, France) were used in this study. As previously described [17,21], the right Achilles tendons were transected after removal of the plantaris tendon and allowed to heal for 1, 2 or 3 weeks. The animals were randomly assigned into two groups, as previously described [17]; 1) full loading (FL) through free cage activity and 2) unloading (UL) by injection of Botox into the calf muscles (4 days prior to surgery) in combination with joint fixation using a steel orthosis post-surgery, and used for three different characterization techniques to assess the micro- and nanoscale structural organization (Table 1). The healing Achilles tendons were harvested together with the calcaneal and gastrocnemius soleus muscle complex (calf muscle) as previously described [17], and stored frozen in phosphate buffered solution (PBS). The experiment adhered to the ARRIVE guidelines and to institutional guidelines for care and treatment of laboratory animals and was approved by the Regional Ethics Committee for animal experiments in Linköping, Sweden (ID1424).

2.2. Sample preparation

To remain structurally stable during the long SASTT measurements, tendons measured with both SR-PhC-µCT and SASTT were thawed and fixed in formalin for 48 h, including the muscle complex and calcaneal bone. Afterwards, the central part of the tendons was cut, leaving the full diameter of the callus but not the full length. Kapton tubes (Goodfellow Cambridge Ltd., UK) were sealed at the bottom with epoxy and filled with 70 % ethanol. The central parts of the tendons were placed in the center of the tubes, which were then sealed at the top by custom made silicon plugs and further reinforced with epoxy (Supporting Information, Fig. S1.A). The Kapton tubes were mounted on needles and put in a brass pin, with the top of the intended field of view (FOV) at a mounted height of 35 mm. As an intact reference and for evaluation of radiation damage during SASTT measurements, two intact contralateral tendons were also harvested and prepared in the same way. For 2D SAXS measurements, tendons including the muscle complex and calcaneal bone were thawed and placed in pockets made of Kapton film (8 µm, 3512, SPEX Sample Prep, USA) filled with PBS.

2.3. Phase-contrast enhanced synchrotron X-ray microtomography

2.3.1. Measurements

SR-PhC-µCT measurements were conducted at the X02DA TOMCAT beamline at the Swiss Light Source (SLS), Paul Scherrer Institute (Villigen, Switzerland) [41]. The projections were acquired using a high numerical aperture microscope setup (4x magnification,

Table 1
Experimental setup. Number of healing tendons used for the three different characterization techniques per loading group (FL and UL). SASTT and SR-PhC-µCT measurements were performed on the same healing tendons, as indicated by *. 2 intact tendons from the contralateral side (exposed to full loading) were used for SASTT measurements; 1 as reference and 1 to assess potential radiation damage.

Characterization technique	1 week	2 weeks	3 weeks	Intact
SR-PhC-µCT (3D microstructure)	1*	–	1*	–
SASTT (3D nanostructure)	1*	–	1*	2
SAXS (2D nanostructure)	4	4	4	–
Histology	1*	–	–	1*

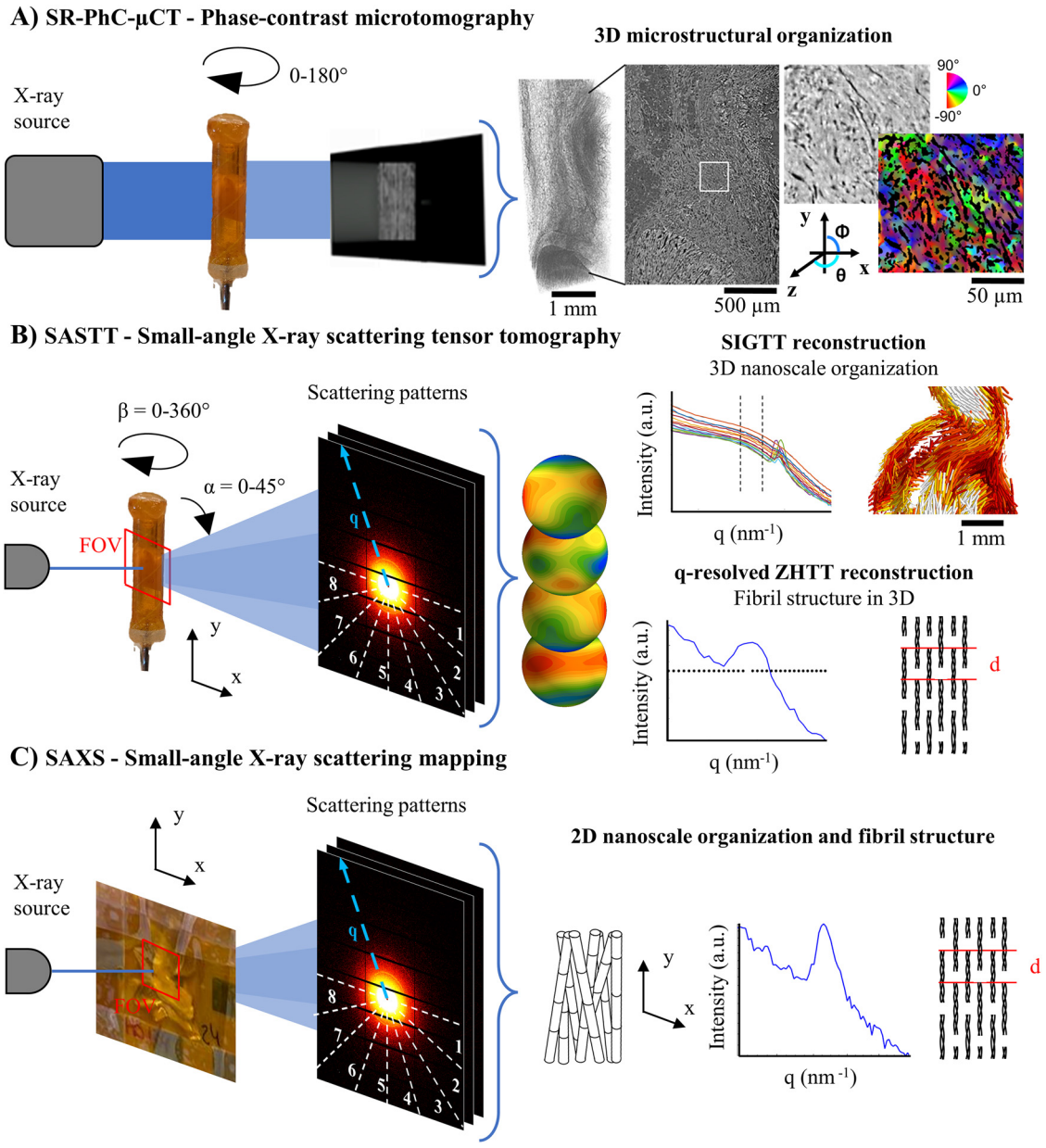

Fig. 1. Overview of experimental techniques and analysis. A) Healing tendons were measured with SR-PhC-µCT. Fiber orientation at the microscale was determined through structure tensor analysis. B) SASTT measurements were performed by mapping the same samples at several rotation and tilt angles. Spherical integral geometric tensor tomography (SIGTT) was used to evaluate the fibril orientation from the q-region related to the collagen fibril diameter scattering and the zonal spherical harmonics method (ZHTT) was used to evaluate fibril structural parameters from the 3rd collagen fibril peak. C) SAXS 2D mapping measurements were performed on healing tendons. The 3rd collagen peak was analyzed for fibril organization and structural parameters.

FOV of 4.2 mm x 3.5 mm and a pixel size of 1.63 µm). The optical setup was coupled to a 150 µm LuAG:Ce scintillator screen. The propagation distance was 150 mm, the X-ray energy was set at 15 keV and 2001 projections were acquired over 180° of continuous rotation [35]. The exposure time was 33 ms resulting in about 90 s scans. 3–8 scans were acquired to cover the full sample volumes. The total radiation dose deposited on the sample was estimated to be 26 Gy per scan, resulting in a total dose of 60–180 Gy depending on the sample. This was achieved through estimating the absorbed energy by the sample divided by the sample mass:

$$Dose = \frac{E \cdot I_o \cdot \tau \cdot A}{V \cdot \rho} \cdot N_{proj} \cdot N_{scans}$$

where E is the X-ray energy, I_0 the photon flux (photons/s), τ the exposure time, A the absorption ratio, V the sample volume, ρ the mass density of the sample N_{proj} the number of projections and N_{scans} the number of scans. All projections were corrected with dark and flat-field images. The projected density of the sample was calculated using the Paganin phase retrieval for homogeneous objects [42]. After measurements, tomographic reconstruction of the acquired projections was performed using a Fourier based regridding algorithm [43].

2.3.2. Data analysis

The orientation distribution of collagen fibers at the microscale in the healing tendons was determined in 3D by performing a structure tensor analysis as previously described [12,44,45] using in-house Matlab® (R2022a, MathWorks Inc, USA) codes. Two volumes of approximately 0.3 mm^3 were chosen in the central part of each tendon. The fibers were thresholded from the background

using the Otsu's method [46]. The data was smoothed with a 3D gaussian filter ($\sigma = 4$), and the structure tensor was calculated for each component smoothed with a second 3D gaussian filter ($\rho = 2$). The analysis provided numerical information about the 3D fiber orientation distribution in the form of spherical coordinates. In particular the elevation angle provided information about the orientation (and reorientation during healing) of the fiber main axes longitudinal to the tendon main axes.

2.4. Small-angle X-ray scattering tensor tomography

2.4.1. Measurements

SASTT measurements were performed at the coherent small-angle X-ray scattering beamline (cSAXS) at the Swiss Light Source (SLS), Paul Scherrer Institute (PSI), Switzerland. The Kapton tubes containing the central part of the tendon callus were mounted on a goniometer connected to a stage which could move in the two planes perpendicular to the beam (x,y) and aligned to the center of rotation (Fig. 1.A ii, Supporting Information, Figure S1). Measurements were conducted using a photon energy of 12.4 keV and scattering patterns were recorded using a Pilatus 2 M detector (1475×1679 pixels^2, pixel size 172×172 μm^2 [47]) at a sample to detector distance of ~7.1 m, providing a q-range of approximately 0.02 to 1.45 nm^{-1}. The tendons were mapped in x and y using a beam and step size of 150×150 μm^2 with an exposure time of 30 ms at 6 equally spaced tilt angles α between 0 and 45° in the z-plane (direction of the beam) and at rotation angles β around the y-axis (Fig. 1.A ii). At $\alpha = 0°$, β was equally spaced between 0 and 180° and at $\alpha \neq 0°$ between 0 and 360° To ensure equal angular sampling independent of tilt angle, the number of projections acquired at $\alpha \neq 0°$ were reduced by a factor of $\cos(\alpha)$ [25,26]. The sample to detector distance and beam center were determined using a silver behenate powder standard. A beamstop was used to block the directly transmitted beam and the beam flux (~2e10 photons/s) was measured using a glassy carbon standard specimen [48]. In order to avoid saturation of the detector, the incoming flux was reduced by reducing the gap of the upstream slits, placed at about 12 m from the source, and by detuning the undulator gap. A diode measuring sample transmission mounted on the beamstop failed during part of the experiment and was therefore only working for one tendon. The individual experimental parameters for each tendon are provided in the Supporting Information (Table S1).

2.4.2. Radiation damage

To evaluate the effect of radiation dose, a measurement of 400 repeated SAXS exposures with an exposure time of 30 ms in one spot was conducted on an intact tendon, representing a total exposure time of 12 s. During this exposure, no systematic effects on the collagen structural parameters were found (Supporting Information, Fig. S2.A). The total dose during this test was estimated as previously described [24], by dividing the absorbed energy in the exposed volume with the sample mass:

$$Dose = \frac{E \cdot I_0 \cdot \tau \cdot A}{\Delta_x \Delta_y \Delta_z \cdot \rho} \cdot N$$

where E is the X-ray energy, I_0 the photon flux (photons/s), τ the exposure time, A the absorption ratio (1-transmission) normalized by air, $\Delta_x\Delta_y\Delta_z$ the scattering volume (beam area × sample thickness), ρ the mass density of the sample (1120 kg/m^3 [49]) and N the number of exposures. The dose rate on this sample was found to be approximately 390 Gy/s, resulting in a dose per exposure and total dose during the test of 12 Gy and 4.7 kGy, respectively.

Additionally, the total dose during the SASTT measurements was estimated similarly on the healing tendon with transmission data. For this, we considered the total absorption of the entire illuminated sample within the first projection, the full sample volume and N as the total number of projections. The dose rate on this sample was found to be approximately 174 Gy/s, resulting in a dose per projection and total dose during the SASTT measurement of 5 Gy and 1.5 kGy, respectively. One projection at $\alpha = 0°$, $\beta = 0°$ was conducted in-between each tilt angle per measurement and afterwards compared for potential radiation induced changes, but no substantial changes were identified (Supporting Information, Fig. S2.B).

2.4.3. Data analysis

The beam stop, dead or over-exposed pixels and gaps between detector modules were masked away from all scattering patterns. The scattering patterns were divided into 16 segments and integrated using the cSAXS Matlab® (R2021a, MatchWorks Inc, USA) package [50]. All projections were visually inspected for potential artefacts, due to *e.g.* beam loss, and if so, excluded from the dataset. Since transmission correction is crucial to properly interpret scattering data from samples with density variations, a procedure to simulate transmission data was developed based on the sample which had transmission measurements (see Supporting Information, Methods). The simulated transmission produced substantially more accurate reconstructions compared to no transmission correction, especially within the callus (Supporting Information, Fig. S3).

To evaluate fibril orientation, the 2D scattering projections were aligned in the range $q = 0.07$ – 0.085 nm^{-1} related to the first collagen fibril diameter scattering shoulder (Fig. 1.B) using an iterative alignment method [51]. Following alignment and transmission correction of the 2D scattering projections, the reciprocal space map in each voxel was reconstructed as band-limited functions on the unit sphere in a representation of even-degree spherical harmonic basis functions $Y_{\updownarrow}^{m}$ up to $\updownarrow_{max} = 6$ and $m \leq |\updownarrow|$, using the recently developed method spherical integral geometric tensor tomography (SIGTT) [52] with the software package MUMOTT [53]. To evaluate the quality of the reconstructions, the 2D intensity, orientation and degree of orientation were visually compared between the measured and synthetic projections. As described in further detail by Nielsen et al. [52], the synthetic projections were calculated from the reconstruction by computing the X-ray transform for each reconstructed coefficient across all measurements, and then mapping those coefficients to the detector segment measured at each rotation and tilt angle. The isotropic component (symmetric scattering intensity), main orientation of the collagen fibrils and their relative anisotropy were extracted from the reconstructed reciprocal space map per voxel. The relative anisotropy was estimated as the standard deviation of the reciprocal space map amplitude over the sphere, normalized by the mean amplitude.

To evaluate fibril structural parameters, the 2D scattering projections were aligned in the range $q = 0.26$ – 0.31 nm^{-1} related to the third collagen fibril axial scattering peak (Fig. 1.B), using an iterative alignment method [51]. To reconstruct one-dimensional scattering intensity curves as a function of q in each voxel, the zonal spherical harmonic (ZHTT) method [25,26,29] was used with the band-limit set to $\updownarrow_{max} = 0$ in 32 linearly spaced q-bins, yielding an isotropic (*i.e.*, orientationally independent) spherical function. In order to improve the signal-to-noise ratio, the 2D scattering projections were down-sampled spatially by a factor of 2 in each scanning direction prior to reconstruction. The third collagen scattering peak in the I(q) curves was fitted with a Gaussian. From the peak fit, the peak position (fibril d-spacing), peak area (relative fibril amount) and peak FWHM (dispersion in axial stagger of collagen fibrils) were estimated using in-house Matlab® (R2021a, MathWorks Inc, USA) codes [21,54]. To obtain the d-spacing and axial stagger dispersion, the peak position and FWHM were con-

verted from reciprocal space (q, nm^{-1}) to real space (D, nm). Details on postprocessing after both reconstruction methods can be found in the Methods section in Supporting Information.

2.5. Small-angle X-ray scattering

2.5.1. Measurements

2D SAXS mapping measurements were carried out at the coherent small-angle X-ray scattering beamline (cSAXS) at the Swiss Light Source (SLS), Paul Scherrer Institute (PSI), Switzerland. The samples were placed on a metal grid mounted on a motorized stage which could move in the two planes perpendicular to the beam. SAXS measurements were conducted using a beam energy of 12.4 keV and scattering patterns were recorded using a Pilatus 2 M detector (1475×1679 $pixels^2$, pixel size 172×172 μm^2 [47]) at a sample to detector distance of ~7.1 m, providing a q-range of approximately 0.02 to 1.45 nm^{-1}. The samples were scanned using a beam and step size of 50×40 μm^2 (horizontal x vertical) and an exposure time of 30 ms. The sample to detector distance and beam center were determined using a silver behenate powder standard. The beam was focused on to the sample and a beamstop was used to block the directly transmitted beam. The beam flux was measured (~2.5e11 photons/s) using a glassy carbon standard specimen [48]. A diode mounted on the beamstop recorded the sample transmission, which was used to correct the scattering signal.

2.5.2. Data analysis

The beam stop, dead or over-exposed pixels and gaps between detector modules were masked away from all scattering patterns. The scattering patterns were divided into 16 segments and integrated using the cSAXS Matlab® (R2021a, MatchWorks Inc, USA) package [50]. The predominant orientation of the collagen fibrils was determined from the 16 integrated angular increments in the range q = 0.276 – 0.306 nm^{-1}, and the degree of orientation was estimated as the ratio between the area under the anisotropic peaks in the I(θ) curves compared to the total scattering [55]. The I(q) scattering curves used to extract collagen structural parameters were obtained in the range q = 0.05 – 1.45 nm^{-1} by radial integration over 360° using in-house Matlab® (R2021a, MatchWorks Inc, USA) codes [21,54]. A Gaussian curve was fitted to the third collagen scattering peak and fibril d-spacing (peak fit position), relative amount (peak fit area) and axial stagger dispersion (peak fit FWHM) were extracted. All collagen parameters were masked based on a minimum peak area to remove background pixels.

For further analysis, two tendons (from UL group; 1 w and 2 w) were excluded as their measured FOV unfortunately did not cover the region of interest. Area analysis was conducted in the callus and stumps. For the callus analysis, an average was estimated for all collagen structural parameters within a square region in the center of the callus between the stumps, with equal sides of half the sample-specific stump-to-stump distance. For the stump analysis, if stumps were present within the scan, representative regions were chosen primarily from the proximal stump, when possible, otherwise the distal. Vertical profiles were obtained between the stumps and averaged over a width of half the stump-to-stump distance. All profiles were normalized by the distance between stumps before averaging, resulting in profiles ranging from 0 (distal stump) to 1 (proximal stump). Horizontal profiles were obtained from the extent of callus present within the scan. All profiles were averaged over a height of half the stump-to-stump distance and then aligned to the central position of the stumps before averaging within groups. As the size of the callus varied over time points and loading groups, the measured regions were not standardized but instead averaged across ± 2 mm from the center of the callus between the stumps.

2.5.3. Histology

For Masson-Goldner histological staining, samples were dehydrated in a series of ethanol solutions and embedded in paraffin. Longitudinal sections (5 µm thick) were cut. Sections were deparaffinized and then rehydrated in an opposite graded series of ethanol. Sections were stained with Weigert's hematoxylin iron solution (5 min) followed by azophloxin staining for 10 min. Samples were washed in 1 % acetic acid and placed in acid orange G solution (1 min). They were then rinsed in 1 % acetic acid, and stained with light green (2 min), then rinsed again in 1 % acetic acid followed by dehydration and xylene clearing and mounting. Imaging was performed with an Olympus BX43 light microscope.

2.5.4. Statistics

Mean, standard deviation (SD) and 95 % confidence intervals (CI) were calculated from 2D SAXS measurements. Two-way ANOVA for unbalanced design was used in the callus and stump regions for the 2D analysis to test the effect of *in vivo* loading scheme (FL *vs* UL) and healing time (1, 2, 3 weeks). Multiple comparison post-hoc test was conducted when appropriate.

3. Results

3.1. 3D organization of healing tendon tissue at the micro- and nanoscale

UL healing tendon calluses had smaller diameters than FL tendons (Figs. 2 and 3). Data obtained by SR-PhC-µCT showed generally less collagenous material at the microscale (newly formed fibers) in UL tendons at both investigated time points (Fig. 2.A, light grey). Instead of collagen fibers, a large part of the callus volume in UL tendons consisted of adipose tissue extending asymmetrically on one side of the callus and in between growing fibers (Fig. 2.A, black spheres, Supporting Information, Fig. S4-S5). In FL tendons adipose tissue was mainly present as a thin layer on one side of the callus and between forming fibers (Fig. 2.A-B). At 3 weeks of healing, fiber regeneration was still confined to a small region in UL tendons, whereas in FL tendons fiber formation occurred in multiple islands surrounded by adipose tissue and vascularization (Fig. 2.A-B).

The stumps were only included in the FOV in UL tendons, as UL tendons generally have shorter stump-to-stump distance compared to FL tendons (Fig. 2 and Fig. 3.A, asterisks). In these UL tendons, integration between the stump and callus tissue was observed (Fig. 2.C, Supporting Information Video S1). These findings were confirmed by histology (Supporting Information, Fig. S4–6). After 1 week, integration was minor and only occurred on the side of the stump. By 3 weeks, the bridging between stump and callus tissues was more substantial as the fibers at the border of the stump were integrated with the surrounding healing tissue, becoming less dense and oriented (Fig. 2.C, arrowheads). However, a sharp transition between stump and healing tissue was still visible on the upper side of the stump, at the transection surface (Fig. 2.C, arrows).

Nanoscale data obtained by SASTT also showed that UL tendons had less collagenous material, as the volumes exhibiting scattering signal from collagen fibrils were smaller. UL tendons had a more folded organization between the stumps, with some parts of the newly formed fibrils being oriented perpendicularly to the long axis of the tendon (Fig. 3.A, Supporting Information Video S2). Additionally, UL tendons exhibited low scattering intensities (Fig. 3.B-C), which had not increased after 3 weeks as in FL tendons. All healing tendons were however within a similar range of scattering intensity as the intact reference. The d-spacing and axial stagger dispersion within the healing tissue remained similar throughout healing time for the UL tendons, while they increased between 1

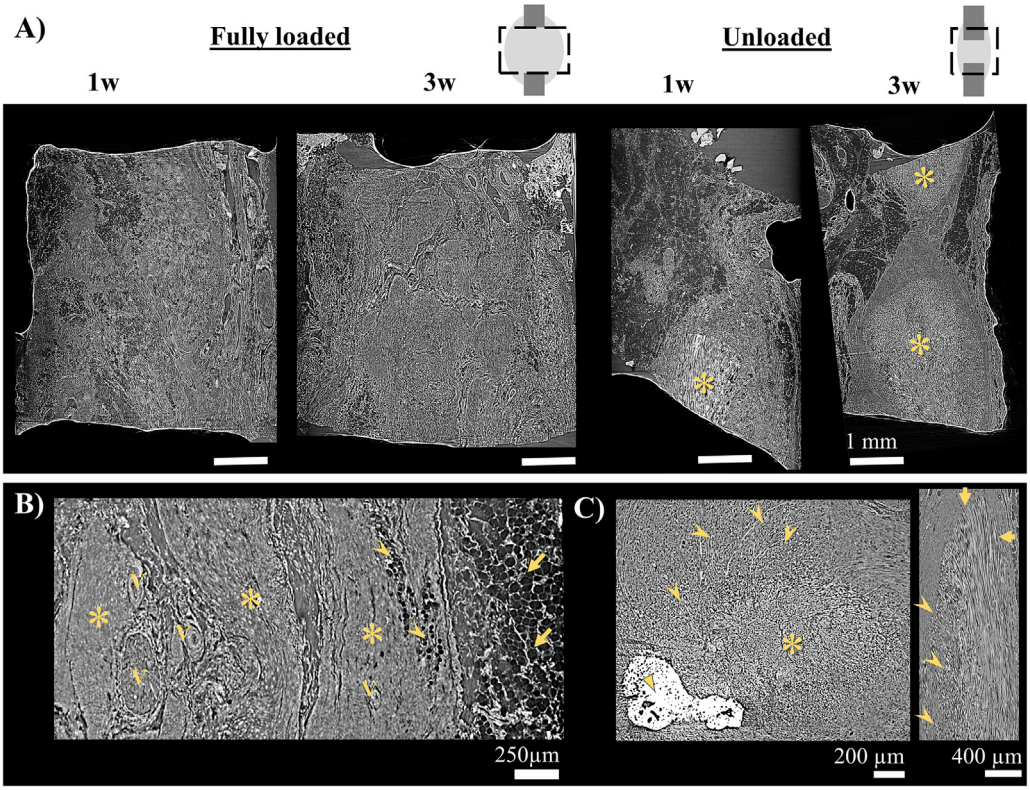

Fig. 2. Visualization of microscale organization of healing tendons by SR-PhC-µCT. A) Central longitudinal views of healing tendons at 1 and 3 weeks exposed to full loading (FL) or unloading (UL), showing the microscale organization of the collagen fibers, adipose tissue and blood vessels. Intact stumps are visible (*) in the UL tendons. B) Compartments of forming fibers (*), blood vessels (v) and adipose tissue within (arrowheads) and on the side (arrows) of the 3 weeks FL healing tendon. C) Signs of integration of the stump with surrounding callus tissue in the 3 weeks UL healing tendon, occurring at one lateral side of the stump (arrowheads), but not on the upper side on the stumps (arrows). A calcified deposit was present in the lower stump (triangle).

and 3 weeks of healing in FL tendons (Fig. 3.C). However, neither UL nor FL tendons reached the same d-spacing as the intact tendon of 66.6 ± 0.5 nm (Fig. 3.C, Supporting Information Fig. S7), and both had higher axial stagger dispersion compared to the intact tendon.

Both fibers and fibrils in UL healing tendons as observed by SR-PhC-µCT and SASTT respectively, were less longitudinally oriented along the tendon main axis and more disorganized compared to the FL tendons (Fig. 4), with UL tendons exhibiting a wider spread in fiber and fibril orientations. After 1 week of healing, the spatially averaged reciprocal space maps within the callus sub-volumes contained multiple intensity maxima (Fig. 4.B), which is a sign of multiple fibril orientations being present within the probed volume. As healing progressed to 3 weeks, both fibers and fibrils became more homogeneously organized and aligned in both UL and FL tendons. The fiber angular distribution narrowed (Fig. 4.C) and the intensity distribution of the averaged reciprocal space maps moved towards only one intensity maxima, *i.e.* one predominant fibril orientation (Fig. 4.B), approaching the ring-like intensity distribution observed in the intact tendon (Supporting Information, Fig. S7.C). The average fibril alignment within the callus tissue did, however, not increase in unloaded tendons after 3 weeks as in fully loaded, and neither of the healing tendons reached the alignment of the intact tendon during this time (Fig. 4.C). After 3 weeks of healing, fiber and fibril organization in the UL tendon had reached an organization resembling that of the FL tendon at 1 week.

3.2. 2D organization of healing tendon tissue at the nanoscale

Initially at one week of healing, most collagen parameters in the callus were similar for UL and FL tendons (Fig. 5 and Fig. 6.A). As healing progressed, the increase in fibril d-spacing was delayed in UL tendons compared to FL, and consequently was substantially lower after 2 and 3 weeks of healing in UL compared to FL tendons (Fig. 6.A i). UL tendons had a more localized presence of high fibril content, compared to FL tendons in which the fibrils were more homogenously distributed (Fig. 5.B). However, the average amount of fibrils in the center of the callus was similar between the two groups and both showed a slightly higher fibril content towards the posterior part of the callus (Fig. 5.B, left side). Initially, axial stagger dispersion was lower in the callus of UL tendons, but after 3 weeks the values were comparable to those of FL tendons (Fig. 5.C and Fig. 6.A iii). Unloading resulted in localized regions with higher degree of orientation, but otherwise no clear differences from FL tendons in orientation and degree of orientation were found within the callus (Fig. 5.D-E and Fig. 6.A iv).

Profile analysis showed structural differences between FL and UL healing tendons which were most pronounced at 2 weeks of healing in the case of all the considered parameters. Fibril d-spacing was higher towards the stumps in both groups, being lowest in the center of the callus (Fig. 6.B i). As the healing progressed, however, the vertical distribution became more homogenous. Both groups initially had a homogenous horizontal distribution across the callus, but as healing progressed, the d-spacing increased towards the core. This increase was delayed in UL compared to FL tendons (Fig. 6.C i). In UL tendons, the vertical distribution of collagen content was similar across the callus, whereas it was higher close to the stumps in FL tendons, being the highest towards the distal stump (Fig. 6.B ii). UL tendons had generally higher fibril content in the callus core at all healing time points (Fig. 6.C, ii), whereas FL tendons progressed from having less to more content within the core and ultimately after 3 weeks of healing a homoge-

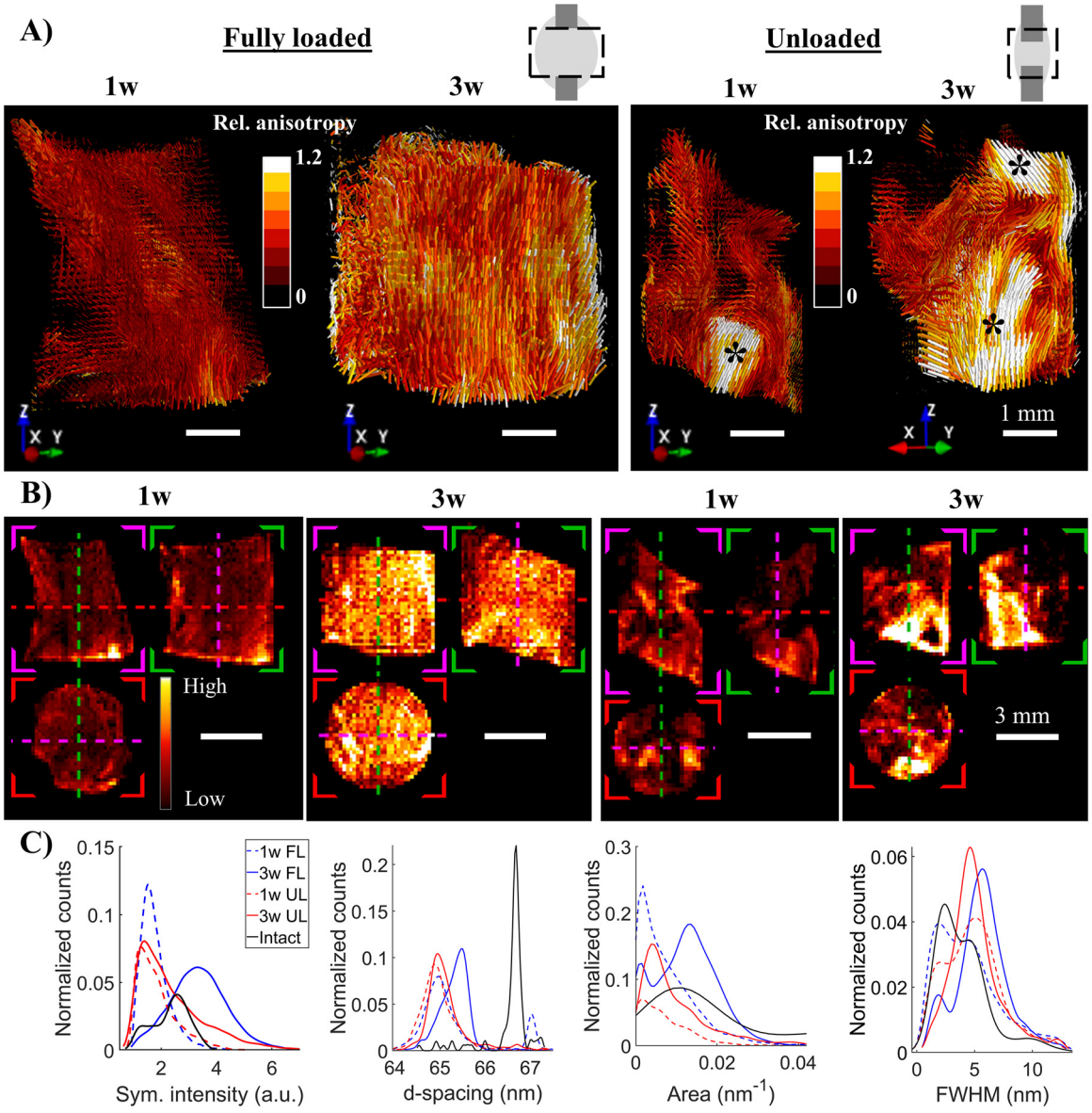

Fig. 3. Visualization and quantification of nanoscale organization of healing tendons by SASTT. A) Glyph render at a longitudinal central cut plane of healing tendons at 1 and 3 weeks exposed to full loading (FL) or unloading (UL) during healing, reconstructed using SIGTT (band-limit $\ell \leq 6$), showing the main orientation (glyph direction), mean scattering intensity (glyph size) and relative anisotropy (STD, color scale) of the nanoscale collagen fibrils. Intact stumps were visible (*) in UL healing tendons. B) Mean scattering intensity (color scale) from the three central cut planes. Colormaps were provided by colorcet.com [56]. C) Histograms of normalized distributions of mean scattering (symmetric) intensity, fibril d-spacing, amount (area) and axial stagger dispersion (FWHM) within the healing tissue compared to the intact tendon reference.

nous horizontal distribution across the callus. Initially, the axial stagger dispersion was also larger close to the stumps, becoming more vertically homogenous as healing progressed in both groups (Fig. 6.B iii). This change was delayed in UL compared to FL tendons. UL tendons showed different horizontal trends in axial stagger dispersion at different weeks, whereas the FL distribution remained relatively homogenous across the callus (Fig. 6.C iii).

UL tendons exhibited a significantly shorter distance between stumps compared to FL tendons (Fig. 5). However, the distance between the stumps decreased with healing time in both groups (FL: 6.0 ± 1.4 mm → 4.6 ± 1.2 mm; UL: 2.0 ± 1.0 mm → 0.8 ± 0.3 mm). As opposed to FL tendons, the stumps within UL tendons remained clearly distinguishable from the surrounding callus in all analyzed collagen parameters (Fig. 5). Within the stumps, changes in d-spacing in UL tendons were minor, whereas in FL tendons the d-spacing decreased over time, approaching the same values as seen in the callus at 3 weeks (Fig. 5.A and Fig. 6.A i). No clear change in axial stagger dispersion was observed in the stumps of UL tendons, whereas it became more homogenous and increasingly similar to the callus in the FL stumps over time. There was no difference in fibril content within the stumps of neither group. The degree of orientation within the stumps of UL tendons remained high, whereas those of FL tendons became more similar to the callus.

4. Discussion

In this study, the effect of the *in vivo* loading environment during rat Achilles tendon healing was thoroughly characterized using a multimodal and multiscale approach. To our knowledge, this study is the first using SASTT to probe soft collagenous tissues and thus provides proof of concept for future investigations in not only tendons, but other non-mineralized collagenous tissues as well. Furthermore, this study demonstrated the sensitivity of SASTT as

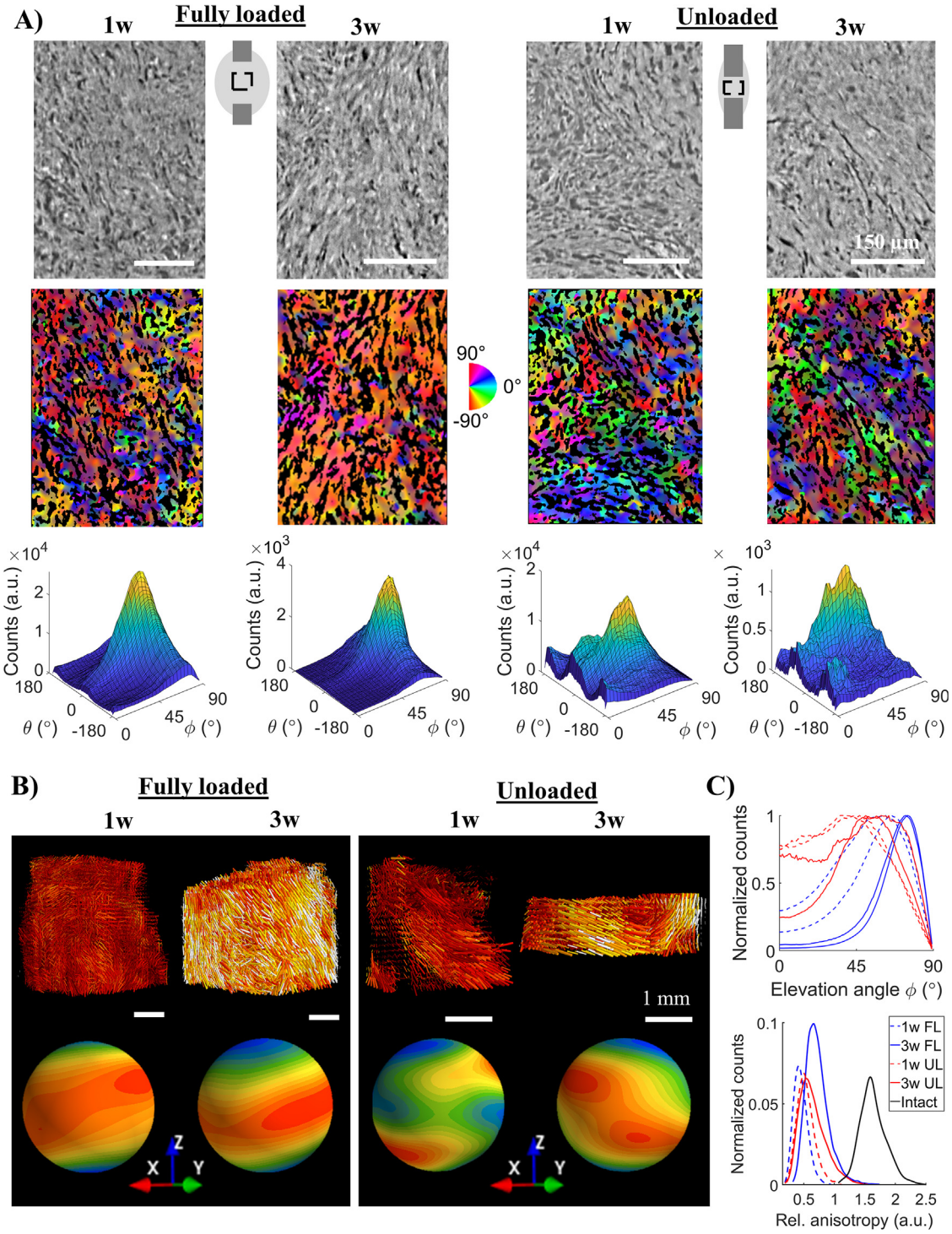

Fig. 4. 3D fiber and fibril orientations in healing tendons by SR-PhC-µCT and SASTT. A) Representative longitudinal 2D slices from a fiber rich volume within the callus, showing the fibers and their orientations (colormap) at the microscale as well as 3D histograms of azimuth (θ, transverse plane) and elevation angles (ϕ, longitudinal plane) for one of the sub-volumes for each group. B) 3D intensity distribution of spatially averaged reciprocal space maps related to fibril scattering from sub-volumes within the central callus region. Colormaps were provided by colorcet.com [56]. C) Normalized histogram of the fiber elevation angle as well as normalized distribution of relative anisotropy of fibrils.

a non-destructive technique to detect collagen fibril amount and structural organization in soft collagenous tissues.

To capture the highly spatially heterogeneous regeneration of collagen during Achilles tendon healing, the micro- and nanostructure of the tendon tissues were probed using a combination of cutting-edge high-resolution synchrotron techniques. The results provided insight into the complex 3D internal collagen fiber and fibril formation during early tendon healing, showing that reduced loading strongly impacts the newly formed collagen. Reduced *in vivo* loading resulted in less collagen formation and delayed alignment both at the fibril and fiber level, as well as reduced stump-to-stump distance (Fig. 7). The collagen network became more homogeneously organized and aligned along the tendon main axes in both groups as healing progressed, although unloaded tendons did

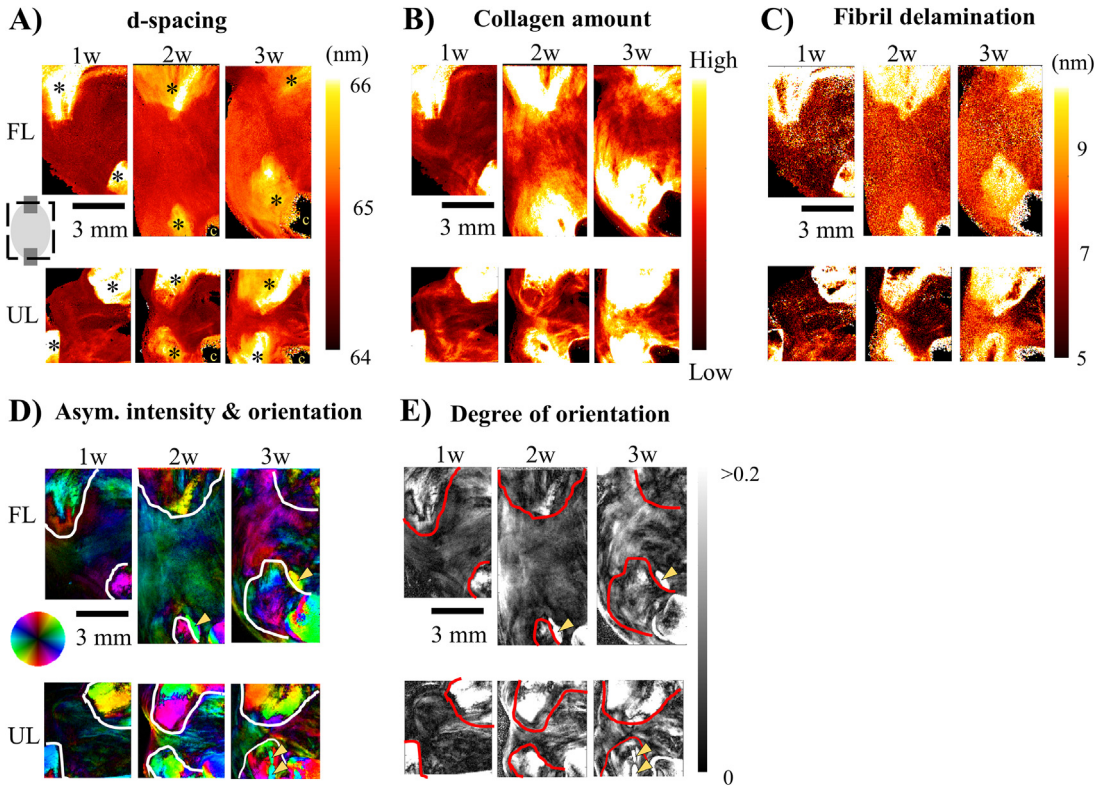

Fig. 5. 2D visualization of nanoscale organization of healing tendon tissue by SAXS. Longitudinal projections of healing tendons exposed to full loading (FL) or unloading (UL) for 1, 2 or 3 weeks of healing. Representative sample maps of A) fibril d-spacing, (* = stumps, c = calcaneal bone), B) fibril amount (peak area), C) axial stagger dispersion (peak FWHM), D) anisotropic scattering (brightness) combined with main orientation (color) (white lines = stumps, arrowhead = calcified deposits) and E) degree of orientation (red lines = stumps, arrowheads = calcified deposits).

not reach the same organization as in fully loaded tendons. At 3 weeks the structural organization of unloaded tendons resembled the one observed in the 1 week fully loaded tendon showing that unloading delays collagen production and alignment but does not prevent this process. The structural changes observed in this study are most likely one of the reasons behind the impaired mechanical properties due to immobilization reported in previous studies of tendon healing [4,15,16,21].

Comparisons with 2D SAXS and SR-PhC-μCT revealed that SASTT can accurately capture the distribution, organization and structure of the collagen fibrils in tendons. Furthermore, this study demonstrates that SASTT is sensitive enough to accurately capture this even as early as at 1 week of tendon healing, at which point the newly formed collagen fibrils are very few, immature and highly disorganized. In general, however, the 2D orientation maps are more difficult to interpret than the 3D data. For example, in some regions of the stumps the fibrils were expected to all be oriented along the main axes of the stumps but instead exhibit almost perpendicular orientations. One reason behind this could be that 2D measurements cannot differentiate among the different planes as the recorded scattering signal is an average of all structures across the whole sample thickness. As a result, the potential anisotropy in the third dimension is lost or smeared out. Additionally, Achilles tendons are composed of 3 sub-tendons which twist along the axes and have slightly different orientations (Supporting Information, Fig. S7) [57], which 2D SAXS cannot distinguish leading to an average signal that can change with small spatial distances. Thus, SASTT is not only a powerful tool when studying mineralized tissues [28–32] but also proved to be a reliable option when studying collagen-rich non-mineralized tissues with complex architectures. SASTT requires minimal invasive sample preparation which enables further complementary investigations or processing of the same samples, while still providing an extensive characterization of the tissue across the entire 3D object. In this study, the limited sample preparation allowed us to image them in liquid instead of introducing further risk of damage by embedding them.

SASTT and SR-PhC-μCT provided complementary insight into the complex hierarchical 3D structure of Achilles tendons, allowing to probe in the same samples how the healing proceeds at fibril level and fiber level, respectively. SASTT provided quantitative information about the collagen fibril formation and its organization at nanoscale. SR-PhC-μCT imaging further enabled us to interpret some of the information provided by SASTT, such as the presence of adipose tissue in regions where no collagen fibrils were detected by SASTT, mineralized deposits at the lower stump periphery and stump integration with the surrounding callus tissue at the fiber level. The stump integration and the presence of adipose tissue were also confirmed by histology (Supporting Information, Fig. S5-S6). All together this multimodal approach offers a better understanding of the process by which fibrils and fibers form and reorient during tendon healing and how this is affected by mechanical stimulation or lack of it.

Delayed formation and maturation of the healing tissue in unloaded tendons were observed as consistently less collagenous tissue within the callus at all time points compared to fully loaded tendons, as well as a reduced fibril d-spacing and axial stagger dispersion. Similar effects have been observed from partially reduced loading of tendons by Botox injections, studied by 2D SAXS and histology [21]. Normal cage activity during rat Achilles tendon healing, has previously been studied by other 2D techniques, showing that collagen does not form with the same structural parameters as intact tissue, but that it matures throughout the healing process. For instance, it has been observed that at the newly formed microscale fibers are thinner than the fibers in the stump

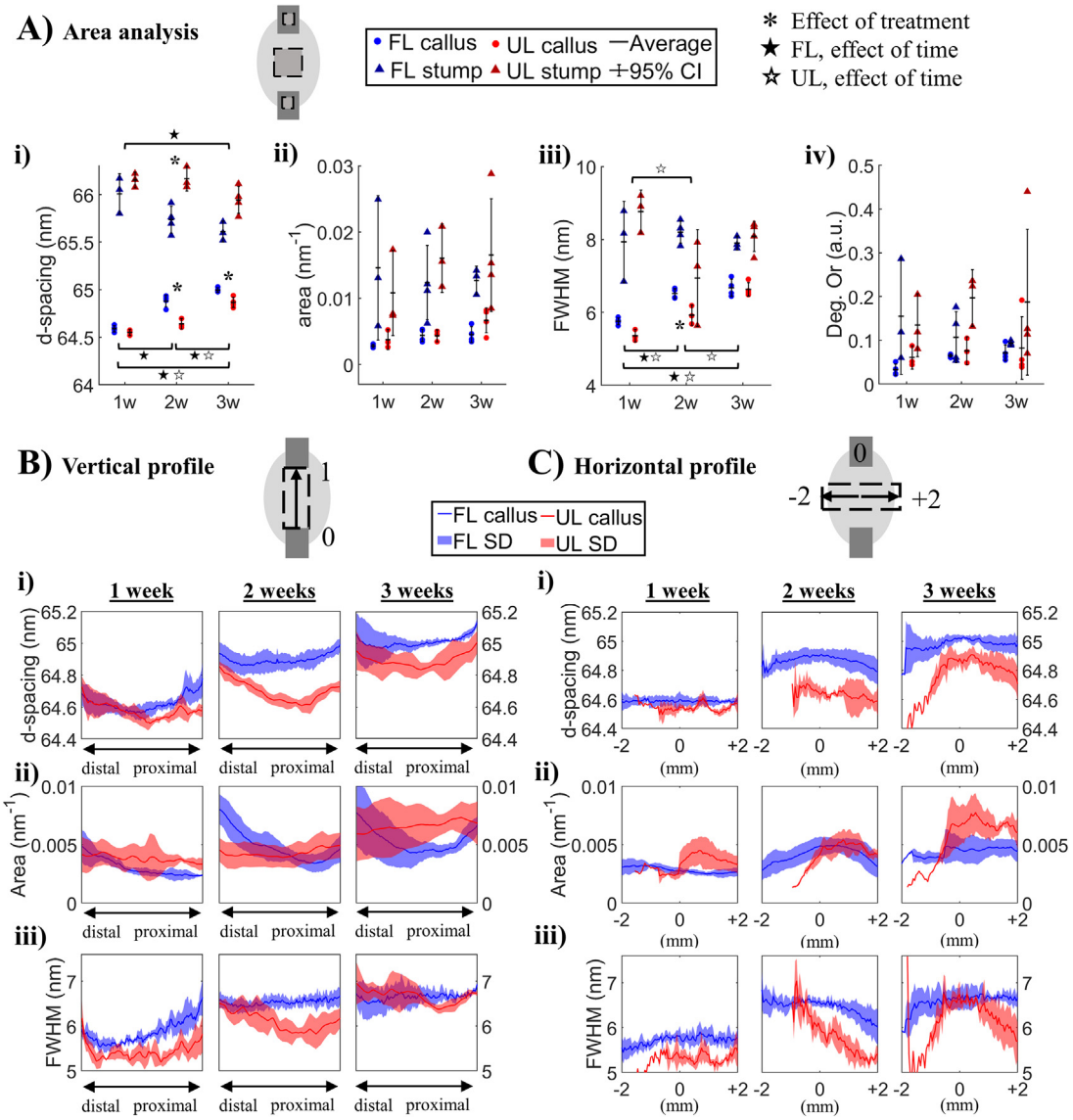

Fig. 6. 2D quantification of collagen fibrils in the healing tendon by SAXS. A) Average fibril degree of orientation (i), d-spacing (ii), amount (peak area, iii) and axial stagger dispersion (peak FWHM, iv) in the center of the callus (dots) and stumps (triangles). Statistically significant differences ($p < 0.05$) are indicated as shown in the legend. B) Vertical callus profiles (normalized to the distance between stumps) and C) horizontal callus profiles (absolute distances) of the fibril structural parameters.

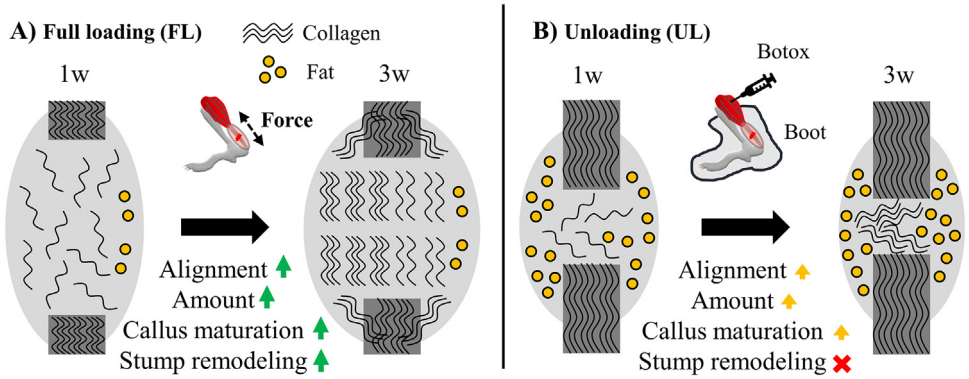

Fig. 7. Schematic representation of the main observations found during early Achilles tendon healing. Summary of findings observed in A) fully loaded (FL) and B) unloaded (UL) tendons. Reduced *in vivo* loading during the early healing process of 1 to 3 weeks resulted in a more disorganized collagen network. Additionally, it led to a shorter distance between the stumps and smaller callus size with less collagen formation and a higher presence of adipose tissue. Independent of loading scheme, both fiber and fibril alignment as well as amount increased over 3 weeks of healing. Compared to full loading, unloading resulted in a delayed maturation of callus fibril properties, as well as no remodeling within the stumps during the investigated time period of 3 weeks.

and that the random initial collagen network becomes more organized as healing progresses [58,59]. These observations are well in line with the findings in the current study. We saw that structural maturation also occurs at the nanoscale, as the d-spacing of newly formed fibrils is initially smaller than in intact tissue, and that it increases during the healing process. Furthermore, the collagen structure became more aligned with healing time at both fiber and fibril levels independently of the loading regime *in vivo*.

Unloading *in vivo* seems to result in delayed remodeling of the remaining tendon stumps. At the microscale, some indications of bridging between the stumps and the callus tissue were observed in unloaded tendons and the process seemed to advance from slight interconnection on the sides at 1 week to conspicuous integration between stump and callus in all directions by 3 weeks. The bridging between callus and stump tissue was also observed in histology (Supporting Information Fig. S5–6). However, fiber bridging does not seem to occur simultaneously as fibril remodeling of the stumps. In fact, all fibril structural parameters within the stumps of unloaded tendons remained clearly distinct from the surrounding callus with no substantial changes during the healing time investigated. Whereas in fully loaded tendons, fibril structural parameters in the stump approached the values of the maturing callus and the callus-stump borders became less distinguishable over time. This indicates that not only is the callus fibril structure maturing towards intact values, but that the fibrils within the stumps also undergo structural changes, with the fibrils potentially being broken down and reorganized. Our study only extended to 3 weeks post-transection, and in the unloaded tendons the stump remodeling might start later. Thus, further investigation is needed to better elucidate this process at later time points.

The results of this study indicate that the new collagen formation seems to start close to the stumps, particularly on the sides where a higher fibril amount was observed, to then progress during healing into the callus and bridging the gap in-between the stumps. Integration of the stumps with the healing callus tissue primarily at the sides was also clearly observed at the fiber level by SR-PhC-μCT and histology. This succession of events during Achilles tendon healing is similar to the one observed in a study by Sasaki et al. [58], where electron microscopy revealed thicker fibers around the stump which formed an axial arrangement from the sides and into the core region, whereas thinner, more randomly organized fibers in the callus instead progressed from the core to the outer layer. These observations of collagen formation starting in the core of the central callus region is further supported by recent histological studies using a murine flexor tendon healing model [60,61]. In the current study, a spatial preference of the collagen formation towards the posterior side of the callus was also found, independently of the loading regime. Data from SR-PhC-μCT indicate that this asymmetry could be associated with the presence of adipose tissue, which were mostly localized on the anterior side of the callus. The posterior regions with higher fibril amount were also characterized by larger d-spacing and higher degrees of orientation. However, a different trend was found in a previous study by our group [21], where the collagen formation was found to initiate at the periphery of the callus, to then progress into its core. Even if this trend differs from the one observed in the current study as well as by Sasaki et al. [58], it is consistent with what we observed in the regions closer to the stumps. In the study by Khayyeri et al. [21], 2D SAXS maps were acquired approximately in the mid-region of the healing callus and did not contain any stumps. Consequently, in case the data was acquired closer to the stumps the trends would be consistent between studies. Moreover, the rats used in the study by Khayyeri et al. [21] were older (16 weeks) and from a different breeder, which may have an impact on the results and lead to differences between our studies.

Although SASTT has many advantages, there are also drawbacks with the technique. The main disadvantage of SASTT is the very long measurement times, which were 15–20 h in this study compared to 20 min for 2D SAXS measurements (Supporting Information, Table S1). Therefore, as the allocated time provided by synchrotrons is highly limited, SASTT studies generally have a low sample number. The scanning time is determined by the target resolution which is inversely proportional to the sample size. However, the total exposure time (excluding overhead) is currently substantially less than the total SASTT measurement time. In the current study, the total exposure time was 4–6 h, which only accounted for one third of the total measurement times. The main reason behind these long measurements are the limitations of detectors, scanning and rotation stages, and their implementation in the motor controls, which can be improved in the future and thus there is potential to substantially reduce measurement times. With SASTT we imaged the entire width of the healing callus, which restricted the spatial resolution that we could achieve. To accommodate for the low sample number and resolution imaged with SASTT, 2D SAXS with 3 times higher resolution was performed on an increased number of samples. The long measurement times of SASTT requires a higher demand on sample stability, which was solved in this study by fixing the samples and imaging them in liquid to avoid dehydration. Long measurement times and increased exposure also lead to higher risk for radiation damage. However, our radiation damage test prior to the experiment as well as our comparison between projections before measurements, in-between tilts and after the measurements, showed similar X-ray signal and retrieved fibril structural parameters (Supporting Information, Fig. S2), indicating no signs of radiation damage. One disadvantage in this study was the lack of transmission measurements due to the failure of the diode mounted on the beam stop which measures this. Transmission correction is crucial, especially in samples with high spatial variations in density. However, to improve this we conducted transmission correction (albeit simulated) which substantially improved the outcome, especially within the callus where the signal is low (Supporting Information, Fig. S3), highlighting the importance of acquiring transmission signals during SASTT measurements.

5. Conclusion

This study represents a proof of concept for future nanostructural investigations using SASTT in non-mineralized collagenous tissues. Furthermore, we provide insights on how reduced *in vivo* loading affects the fiber and fibril formation and maturation during early Achilles tendon healing. The structural differences observed in this study not only provide the foundation for future studies in this direction, but also stress the need for investigations on how structural changes on the micro- and nanoscale affect the mechanical response of the healing tendon.

Declaration of Competing Interest

The authors declare that they have no known competing financial interests or personal relationships that could have appeared to influence the work reported in this paper.

CRediT authorship contribution statement

Isabella Silva Barreto: Conceptualization, Methodology, Investigation, Formal analysis, Validation, Writing – original draft. **Maria Pierantoni:** Conceptualization, Methodology, Investigation, Formal analysis, Validation, Writing – review & editing. **Leonard C. Nielsen:** Methodology, Software, Resources, Validation, Writing –

review & editing. **Malin Hammerman:** Data curation, Methodology, Investigation, Writing – review & editing. **Ana Diaz:** Methodology, Resources, Writing – review & editing. **Vladimir Novak:** Methodology, Resources, Writing – review & editing. **Pernilla Eliasson:** Conceptualization, Validation, Supervision, Writing – review & editing. **Marianne Liebi:** Methodology, Investigation, Software, Resources, Validation, Supervision, Writing – review & editing. **Hanna Isaksson:** Conceptualization, Methodology, Investigation, Validation, Funding acquisition, Supervision, Writing – review & editing.

Acknowledgements

This project has received funding from the Knut and Alice Wallenberg KAW Foundation (Wallenberg Academy Fellows 2017.0221), the European Research Council (ERC) under the European Union's Horizon 2020 research and innovation programme (grant agreement No. 101002516), the Royal Physiographic Society of Lund (41380), the Greta and Johan Kocks foundation (188_20201015_071), the Magnus Bergvall foundation (2020-03683) and the Swedish National Centre for Research in Sports (P2020-0066). L.C.N. and M.L. acknowledge funding from the European Research Council (ERC-2020-StG 949301) for the development of the software package MUMOTT. We acknowledge the Paul Scherrer Institute, Villigen, Switzerland for provision of synchrotron radiation beamtime at TOMCAT and cSAXS, as well as their beamline staff, and Kunal Sharma, Lund University, for helping with histology.

Supplementary materials

Supplementary material associated with this article can be found, in the online version, at doi:10.1016/j.actbio.2023.12.015.

References

[1] T.T. Huttunen, P. Kannus, C. Rolf, L. Felländer-Tsai, V.M. Mattila, Acute Achilles tendon ruptures: incidence of injury and surgery in Sweden between 2001 and 2012, Am. J. Sports Med. 42 (10) (2014) 2419–2423.
[2] I. Lantto, J. Heikkinen, T. Flinkkilä, P. Ohtonen, J. Leppilahti, Epidemiology of Achilles tendon ruptures: increasing incidence over a 33-year period, Scand. J. Med. Sci. Sports 25 (1) (2015) e133–e138.
[3] N.J. Lemme, N.Y. Li, S.F. DeFroda, J. Kleiner, B.D. Owens, Epidemiology of Achilles tendon ruptures in the United States: athletic and nonathletic injuries from 2012 to 2016, Orthop. J. Sport Med. 6 (11) (2018).
[4] T. Notermans, M. Hammerman, P. Eliasson, H. Isaksson, Tendon mechanobiology in small animal experiments during post-transection healing, Eur. Cells Mater. 42 (2021) 375–391.
[5] M.L. Killian, L. Cavinatto, L.M. Galatz, S. Thomopoulos, The role of mechanobiology in tendon healing, J. Shoulder Elb. Surg. 21 (2) (2012) 228–237.
[6] P. Blomgran, R. Blomgran, J. Ernerudh, P. Aspenberg, A possible link between loading, inflammation and healing: immune cell populations during tendon healing in the rat, Sci. Rep. 6 (2016).
[7] J.G. Snedeker, J. Foolen, Tendon injury and repair – a perspective on the basic mechanisms of tendon disease and future clinical therapy, Acta Biomater. 63 (2017) 18–36.
[8] J.F. Maempel, T.O. White, S.P. Mackenzie, C. McCann, N.D. Clement, The epidemiology of Achilles tendon re-rupture and associated risk factors: male gender, younger age and traditional immobilising rehabilitation are risk factors, Knee Surg., Sport Traumatol. Arthrosc. 30 (7) (2022) 2457–2469.
[9] J.H.C. Wang, Mechanobiology of tendon, J. Biomech. 39 (9) (2006) 1563–1582.
[10] M.D. de Boer, A. Selby, P. Atherton, K. Smith, O.R. Seynnes, C.N. Maganaris, N. Maffulli, T. Movin, M.V. Narici, M.J. Rennie, The temporal responses of protein synthesis, gene expression and cell signalling in human quadriceps muscle and patellar tendon to disuse, J. Physiol. 585 (1) (2007 Nov) 241–251.
[11] K. Dideriksen, A.P. Boesen, S. Reitelseder, C. Couppé, R. Svensson, P. Schjerling, S.P. Magnusson, L. Holm, M. Kjaer, Tendon collagen synthesis declines with immobilization in elderly humans: no effect of anti-inflammatory medication, J. Appl. Physiol. 122 (2) (2017) 273–282.
[12] M. Pierantoni, I. Silva Barreto, M. Hammerman, V. Novak, A. Diaz, J. Engqvist, P. Eliasson, H. Isaksson, Multimodal and multiscale characterization reveals how tendon structure and mechanical response are altered by reduced loading, Acta Biomater 168 (2023) 264–276.
[13] M.E. Wall, N.A. Dyment, J. Bodle, J. Volmer, E. Loboa, A. Cederlund, A.M. Fox, A.J. Banes, Cell signaling in tenocytes: response to load and ligands in health and disease. In: Ackermann, P, Hart, D, (eds) Metabolic Influences on Risk for Tendon Disorders Advances in Experimental Medicine and Biology. Vol 920. Springer; 2016. p. 79–95.
[14] G. Riley, Tendinopathy - from basic science to treatment, Nat. Clin. Pract. Rheumatol. 4 (2) (2008) 82–89.
[15] T. Andersson, P. Eliasson, M. Hammerman, O. Sandberg, P. Aspenberg, Low-level mechanical stimulation is sufficient to improve tendon healing in rats, J. Appl. Physiol. 113 (9) (2012) 1398–1402.
[16] L.M. Galatz, N. Charlton, R. Das, H.M. Kim, N. Havlioglu, S. Thomopoulos, Complete removal of load is detrimental to rotator cuff healing, J. Shoulder Elb. Surg. 18 (5) (2009 Sep) 669–675.
[17] M. Hammerman, F. Dietrich-Zagonel, P. Blomgran, P. Eliasson, P. Aspenberg, Different mechanisms activated by mild *versus* strong loading in rat Achilles tendon healing, PLoS One 13 (7) (2018).
[18] P. Eliasson, T. Andersson, P. Aspenberg, Influence of a single loading episode on gene expression in healing rat Achilles tendons, J. Appl. Physiol. 112 (2) (2012) 279–288.
[19] P. Fratzl, Collagen: structure and mechanics, an introduction, in: Collagen, Springer US, Boston, MA, 2008, pp. 1–13.
[20] H. Khayyeri, P. Blomgran, M. Hammerman, M.J. Turunen, A. Löwgren, M. Guizar-Sicairos, P. Aspenberg, H. Isaksson, Achilles tendon compositional and structural properties are altered after unloading by Botox, Sci. Rep. 7 (1) (2017) 13067.
[21] H. Khayyeri, M. Hammerman, M.J. Turunen, P. Blomgran, T. Notermans, M. Guizar-Sicairos, P. Eliasson, P. Aspenberg, H. Isaksson, Diminishing effects of mechanical loading over time during rat Achilles tendon healing, PLoS One 15 (12) (2020) e0236681.
[22] S.R. Inamdar, S. Prévost, N.J. Terrill, M.M. Knight, H.S. Gupta, Reversible changes in the 3D collagen fibril architecture during cyclic loading of healthy and degraded cartilage, Acta Biomater. 136 (2021) 314–326.
[23] S.R. Inamdar, D.P. Knight, N.J. Terrill, A. Karunaratne, F. Cacho-Nerin, M.M. Knight, H.S. Gupta, The secret life of collagen: temporal changes in nanoscale fibrillar pre-strain and molecular organization during physiological loading of cartilage, ACS Nano 11 (10) (2017) 9728–9737.
[24] I. Silva Barreto, M. Pierantoni, M. Hammerman, E. Törnquist, S. Le Cann, A. Diaz, J. Engqvist, M. Liebi, P. Eliasson, H Isaksson, Nanoscale characterization of collagen structural responses to *in situ* loading in rat Achilles tendons, Matrix Biol. 115 (2023) 32–47.
[25] M. Liebi, M. Georgiadis, A. Menzel, P. Schneider, J. Kohlbrecher, O. Bunk, Guizar-Sicairos M. Nanostructure surveys of macroscopic specimens by small-angle scattering tensor tomography, Nature 527 (7578) (2015) 349–352.
[26] M. Liebi, M. Georgiadis, J. Kohlbrecher, M. Holler, J. Raabe, I. Usov, A. Menzel, P. Schneider, O. Bunk, M. Guizar-Sicairos, Small-angle X-ray scattering tensor tomography: model of the three-dimensional reciprocal-space map, reconstruction algorithm and angular sampling requirements, Acta Crystallogr. Sect. A Found. Adv. (2018).
[27] M. Guizar-Sicairos, M. Georgiadis, M. Liebi, Validation study of small-angle X-ray scattering tensor tomography, J. Synchrotron Radiat. 27 (2020) 779–787.
[28] T.A. Grünewald, M. Liebi, N.K. Wittig, A. Johannes, T. Sikjaer, L. Rejnmark, Z. Gao, M. Rosenthal, M. Guizar-Sicairos, H. Birkedal, M. Burghammer, Mapping the 3D orientation of nanocrystals and nanostructures in human bone: indications of novel structural features, Sci. Adv. 6 (24) (2020) 4171–4183.
[29] M. Liebi, V. Lutz-Bueno, M. Guizar-Sicairos, B.M. Schönbauer, J. Eichler, E. Martinelli, J.F. Löffler, A. Weinberg, H. Lichtenegger, T.A. Grünewald, 3D nanoscale analysis of bone healing around degrading Mg implants evaluated by X-ray scattering tensor tomography, Acta Biomater. (2021).
[30] E.A. Casanova, A. Rodriguez-Palomo, L. Stähli, K. Arnke, O. Gröninger, M. Generali, Y. Neldner, S. Tiziani, A.P. Dominguez, M. Guizar-Sicairos, Z. Gao, C. Appel, L.C. Nielsen, M. Georgiadis, F.E. Weber, W. Stark, H.C. Pape, P. Cinelli, M. Liebi, SAXS imaging reveals optimized osseointegration properties of bioengineered oriented 3D-PLGA/aCaP scaffolds in a critical size bone defect model, Biomaterials 294 (2023) April 2022.
[31] F.K. Mürer, B. Chattopadhyay, A.S. Madathiparambil, K.R. Tekseth, M. Di Michiel, M. Liebi, M.B. Lilledahl, K. Olstad, D.W. Breiby, Quantifying the hydroxyapatite orientation near the ossification front in a piglet femoral condyle using X-ray diffraction tensor tomography, Sci. Rep. 11 (1) (2021) 2144.
[32] T.A. Grünewald, A. Johannes, N.K. Wittig, J. Palle, A. Rack, M. Burghammer, H. Birkedal, Bone mineral properties and 3D orientation of human lamellar bone around cement lines and the Haversian system, IUCrJ 10 (2) (2023) 189–198.
[33] A.K. Rajasekharan, A. Lotsari, V. Lutz-Bueno, M. Liebi, M. Andersson, Bioinspired structural hierarchy within macroscopic volumes of synthetic composites, Adv. Healthc. Mater. 7 (18) (2018) 1–7.
[34] M. Georgiadis, A. Schroeter, Z. Gao, M. Guizar-Sicairos, M. Liebi, C. Leuze, J.A. McNab, A. Balolia, J. Veraart, B. Ades-Aron, S. Kim, T. Shepherd, C.H. Lee, P. Walczak, S. Chodankar, P. DiGiacomo, G. David, M. Augath, V. Zerbi, S. Sommer, I. Rajkovic, T. Weiss, O. Bunk, L. Yang, J. Zhang, D.S. Novikov, M. Zeineh, E. Fieremans, M. Rudin, Nanostructure-specific X-ray tomography reveals myelin levels, integrity and axon orientations in mouse and human nervous tissue, Nat. Commun. 12 (1) (2021) 1–13.

[35] M. Pierantoni, I. Silva Barreto, M. Hammerman, L. Verhoeven, E. Törnquist, V. Novak, R. Mokso, P. Eliasson, H Isaksson, A quality optimization approach to image Achilles tendon microstructure by phase-contrast enhanced synchrotron micro-tomography, Sci. Rep. 11 (1) (2021) 17313.
[36] Y. Zhou, J. Hu, J. Zhou, Z. Zeng, Y. Cao, Z. Wang, C. Chen, C. Zheng, H. Chen, H. Lu, Three-dimensional characterization of the microstructure in rabbit patellaâ€"patellar tendon interface using propagation phase-contrast synchrotron radiation microtomography, J. Synchrotron Radiat. 25 (6) (2018) 1833–1840.
[37] T. Zhang, S. Li, Y. Chen, H. Xiao, L. Wang, J. Hu, D. Xu, H. Lu, Characterize the microstructure change after tendon enthesis injury using synchrotron radiation μCT, J. Orthop. Res. 40 (11) (2022) 2678–2687.
[38] E. Einarsson, M. Pierantoni, V. Novak, J. Svensson, H. Isaksson, M. Englund, Phase-contrast enhanced synchrotron micro-tomography of human meniscus tissue, Osteoarthr. Cartil. 30 (9) (2022) 1222–1233.
[39] C.M. Disney, K. Madi, A.J. Bodey, P.D. Lee, J.A. Hoyland, M.J. Sherratt, Visualising the 3D microstructure of stained and native intervertebral discs using X-ray microtomography, Sci. Rep. 7 (1) (2017) 1–11.
[40] A. Horng, J. Stroebel, T. Geith, S. Milz, A. Pacureanu, Y. Yang, P. Cloetens, G. Lovric, A. Mittone, A. Bravin, P. Coan, Multiscale X-ray phase contrast imaging of human cartilage for investigating osteoarthritis formation, J. Biomed. Sci. 28 (1) (2021) 1–14.
[41] M. Stampanoni, A. Groso, A. Isenegger, G. Mikuljan, Q. Chen, A. Bertrand, S. Henein, R. Betemps, U. Frommherz, P. Böhler, D. Meister, M. Lange, R. Abela, Trends in synchrotron-based tomographic imaging: the SLS experience, Dev. X-Ray Tomogr. V 6318 (2006) 63180M September 2006.
[42] D. Paganin, S.C. Mayo, T.E. Gureyev, P.R. Miller, S.W. Wilkins, Simultaneous phase and amplitude extraction from a single defocused image of a homogeneous object, J. Microsc. 206 (1) (2002) 33–40.
[43] F. Marone, M. Stampanoni, Synchrotron Radiation Regridding reconstruction algorithm for real-time tomographic imaging, J Synchrotron Rad 19 (2012) 1029–1037.
[44] M. Krause, J.M. Hausherr, B. Burgeth, C. Herrmann, W Krenkel, Determination of the fibre orientation in composites using the structure tensor and local X-ray transform, J. Mater. Sci. 45 (4) (2010) 888–896.
[45] N. Jeppesen, V.A. Dahl, A.N. Christensen, A.B. Dahl, L.P. Mikkelsen, V. Andersen, C. Himmelstrup, A. Bjorholm, P. Saxena, G. Bissacco, C. Gundlach, V. Andersen Dahl, C. Himmelstrup Trinderup, A Bjorholm Dahl, Process characterization for molding of paper bottles using computed tomography and structure tensor analysis, E-J. Nondestruct. Test Ultrason. 942 (1) (2020) 24.
[46] N. Otsu, A threshold selection method from gray-level histograms, IEEE Trans. Syst. Man Cybern. 9 (1) (1979) 62–66.
[47] P. Kraft, A. Bergamaschi, C. Broennimann, R. Dinapoli, E.F. Eikenberry, B. Henrich, I. Johnson, A. Mozzanica, C.M. Schlepütz, P.R. Willmott, B. Schmitt, Performance of single-photon-counting PILATUS detector modules, J. Synchrotron Radiat. 16 (3) (2009) 368–375.
[48] A.J. Allen, F. Zhang, R. Joseph Kline, W.F. Guthrie, J Ilavsky, NIST standard reference material 3600: absolute intensity calibration standard for small-angle X-ray scattering, J. Appl. Crystallogr. 50 (2017) 462–474.
[49] Ker RF, Dynamic tensile properties of the plantaris tendon of sheep (Ovis Aries), Exp. Biol. 2 (1981).
[50] CXS groupScanning SAXS Software Package, PSI, Switzerland, 2022 Available from: https://www.psi.ch/en/sls/csaxs/software .
[51] M. Odstrčil, M. Holler, J. Raabe, M. Guizar-Sicairos, Alignment methods for nanotomography with deep subpixel accuracy, Opt. Express 27 (25) (2019) 36637.
[52] L.C. Nielsen, P. Erhart, M. Guizar-Sicairos, M. Liebi, Small-angle scattering tensor tomography algorithm for robust reconstruction of complex textures, Acta Crystallogr. Sect. A Found. Adv. 79 (6) (2023) 1–12.
[53] Nielsen L., Carlsen M., Liebi M., Erhart P. MUMOTT software package. 2023. Available from: https://zenodo.org/record/7919490#.ZFyp-XZByUm
[54] M.J. Turunen, H. Khayyeri, M. Guizar-Sicairos, H. Isaksson, Effects of tissue fixation and dehydration on tendon collagen nanostructure, J. Struct. Biol. 199 (3) (2017) 209–215.
[55] O. Bunk, M. Bech, T.H. Jensen, R. Feidenhans'L, T. Binderup, A. Menzel, F Pfeiffer, Multimodal x-ray scatter imaging, New J. Phys. 11 (2009) 1–8.
[56] Kovesi P. Good colour maps: how to design them. 2015;
[57] M. Edama, M. Kubo, H. Onishi, T. Takabayashi, T. Inai, E. Yokoyama, W. Hiroshi, N. Satoshi, I. Kageyama, The twisted structure of the human Achilles tendon, Scand. J. Med. Sci. Sport 25 (5) (2015) e497–e503.
[58] K. Sasaki, N. Yamamoto, T. Kiyosawa, M. Sekido, The role of collagen arrangement change during tendon healing demonstrated by scanning electron microscopy, J. Electron Microsc. 61 (5) (2012) 327–334.
[59] B.R. Freedman, A.B. Rodriguez, C.D. Hillin, S.N. Weiss, B. Han, L. Han, L.J. Soslowsky, Tendon healing affects the multiscale mechanical, structural and compositional response of tendon to quasi-static tensile loading, J. R. Soc. Interface 15 (139) (2018).
[60] K.T. Best, A.E. Loiselle, Scleraxis lineage cells contribute to organized bridging tissue during tendon healing and identify a subpopulation of resident tendon cells, FASEB J. 33 (7) (2019) 8578–8587.
[61] J.E. Ackerman, K.T. Best, S.N. Muscat, E.M. Pritchett, A.E.C. Nichols, C.L. Wu, A.E. Loiselle, Defining the spatial-molecular map of fibrotic tendon healing and the drivers of Scleraxis-lineage cell fate and function, Cell Rep. 41 (8) (2022).